

Biomimetic surface strategy of spectrum-tailored liquid metal *via* blackbody inspiration for highly efficient solar steam generation, desalination, and electricity generation

Zechang Wei, Chenyang Cai, Yangze Huang, Yongqin Wang, Yu Fu ^{*}

Co-Innovation Center of Efficient Processing and Utilization of Forest Resource, School of Materials Science and Engineering, Nanjing Forestry University, Nanjing, Jiangsu 210037, China

ARTICLE INFO

Keywords:

Liquid metals
Lignin aerogels
Solar steam generation
Electricity generation
Desalination

ABSTRACT

Solar steam generation as a promising strategy has attracted more and more attention owing to its applications of the water purification which meet the demand of clean water worldwide. Photothermal material, as the key component of solar evaporators, has aroused great interest in the design of extraordinary photothermal conversion efficiency. Herein, liquid metal was the first time used to develop a photothermal promotor with the tailored spectrum *via* the dipole layer strategy for highly efficient solar steam generation. As the proof-of-concept, cellulose nanocrystals were applied as bonding agent of matrix scaffold and photothermal layer for the successful preparation of the lignin-based aerogel evaporators. Inspired by the seedless sunflower, binary configurations of interior topology and surface topography was manipulated on the layer-doubled lignin-based aerogels with inverted pyramid veneer for the favorable multi-functionalities, which could hardly realize within the entirety before. The blackbody-inspired aerogel evaporators showed exceptional solar evaporation efficiency of 94% under 1 sun, and the depuration and desalination efficiency up to 99% in the sewage (water containing Zn^{2+} , Ni^{2+} , Cu^{2+} , Fe^{3+}) and seawater (Yellow sea, China). In addition, the resulted lignin-based aerogels also presented a promising application in the electricity generation field. This work opens a new avenue to design liquid metals with excellent light absorption ability for the effective solar steam generation, sewage depuration and desalination, with the application of liquid metals in the electricity generation field.

1. Introduction

As one of the most common substances on the earth, water covers 71% of the earth surface [1]. It is the non-substitutable resource for survival of human beings and the most important component of living organisms. With sanitary water-stress gradually emerging as the urgent issue for the world, it is predicted that the two-third of the world's population will fall into the predicament of sanitary water-stress in 2025 [2]. Inevitably the water-stress will lead to economic depression and energy shortage in the world [3]. Since the most hydrological regimes on the earth is sea water, which cannot be directly drunk, various technologies have been exploited for water purification such as fog collection [4,5], membrane treatment [6], advanced oxidation [7] and solar steam generation [2,8]. Among them, solar steam generation has attracted much more attention because solar energy was sustainable and environmentally benign [9]. However, because the sunlight is rather

diffusing and the optical absorption of the sea water is very low, the naturally self-generating photothermal effectiveness is not enough to meet the impending demand to produce fresh water [3]. To realize the optimal solar steam generation, the facile methods are needed to enhance sunlight capture and reduce heat loss to the surroundings for the photothermal efficiency improvement [9]. Integrating the solar steam generation, water purification and electricity generation into one system, which could solve the water-stress and energy shortage simultaneously, have been attracted more and more attention [10,11]. Therefore, recently a number of intensive studies have been made to design the photothermal materials with wide-spectrum light absorption to maximize the sunlight absorption capability. Therefore, the key and essential challenge comes to seek a high-performance photothermal material for the highly efficient solar steam generation, water purification and electricity generation.

Since the development of the high-performance photothermal

* Corresponding author.

E-mail address: fuyu@wsu.edu (Y. Fu).



materials is most imperative for the solar steam generation, a range of photothermal materials have been reported up till now, which can be classified into three categories: carbon-based materials [12,13], noble metal nano-particles [14,15], and semiconductor materials [16,17]. Among them, carbon-based materials presented the excellent photothermal performance and light-to-heat conversion effect, such as graphene [18], carbon nanotubes and carbonized biomass [19]. Jiang et al. reported that the system could achieve 76.3% solar steam generation efficiency under 1 sun, when the bilayer CNF-CNT aerogel was fabricated for solar steam generation [8]. Although carbon materials could efficiently absorb light, their surficial light reflection presented to be an obvious drawback [20]. A range of metals have been studied for highly efficient solar steam generation, such as Au, Ag and Pt [2,15,21]. Some researchers found that plasmonic metals were more effective in harvesting solar light because of the localized surface plasmon resonance (LSPR) effect [22]. However, the narrow light absorption range of these plasmonic metals hindered their potential applications in the field of solar steam generation. As for the narrow-bandgap semiconductor materials, the photothermal performance is determined by their bandgap energy. When the incident light energy higher than the bandgap energy is applied, the electron-hole pairs can be generated and those electron-hole pairs above bandgap would then relax to the band edges. Finally, the extra energy converted into heat [23] such as TiO₂ [24], MoS₂ [25]. For those semiconductor materials with broad bandgap, the bandgap could be further narrowed for the efficient photothermal conversion by doping approach [23]. Therefore, it is urgently desirable to explore a kind of photothermal layer with lower surficial light reflection and wide-spectrum light absorption for solar light harvesting.

Liquid metal has attracted the attention of researchers due to its comparably low price, good fluidity and low toxicity. It has been shown its advantages in variety research fields, such as stretchable devices [26], circuits [27], biomedical [28], owing to its high conductivity, non-toxic and flowability [29]. Although liquid metal has been used in many fields, it has never been used in the applications of solar steam generation due to its weak sunlight absorption property. As a widely reported metal alloy with low melting point near room temperature [29], gallium and indium alloy (EGaIn) was hindered from absorbing the sunlight because of the broad bandgap of the gallium trioxide (Ga₂O₃, a kind of the dielectric layer on the surfaces). As we know, since semiconductors can absorb solar energy at the visible wavelength when their E_g is lower than 3 eV, the photons with energy higher than E_g can be absolutely captured and absorbed when the sunlight irradiates the semiconductors. Therefore, to achieve the goal of the wide-spectrum light absorption of EGaIn, the bandgap of Ga₂O₃ would be necessarily reduced. Until now, the reports on the facile methods to reduce the bandgap of metals and their alloys have never been found for light absorption promotion, except for the TiO₂ bandgap reduction through a dipole layer [30]. Thus, it is of paramount importance in reducing the bandgap of liquid metals for their light absorptivity improvement of solar steam generation.

Recently most studies have been made on the photothermal materials with high thermal conductivity, especially the metal-based photothermal materials. The reduction of thermal conductivity of photothermal materials is essential for high efficiency of solar steam generation. During the light-to-heat process, the sunlight-converted heat energy was partially lost to the air and water, and the efficiency of solar steam generation would be reduced. Therefore, the thermal management performance of solar evaporator is particularly needed for the solar steam generation [31,32]. Several kinds of porous photothermal materials were reported to improve the efficiency of solar steam generation, such as the natural wood [33], foam [34], aerogels [35,36]. Specially, aerogels with low density, ultralow thermal conductivity, and ultrahigh porosity have attracted wide interest in the fields of thermal insulation and water treatment application [8,37]. With the incorporation of aerogels into the solar evaporators, the solar steam generation efficiency of photothermal materials would be improved [38]. Many studies have

proved that the effective evaporators should meet three features: broadband sunlight absorption, low thermal conductivity and rapid water transportation [39]. The sufficient and rapid water transportation of the solar evaporators could be fabricated by the conjugated micro-porous polymer [40] or the polystyrene [41]. However, considering the environment pollution, natural polymer materials have become the top choice to fabricate the solar evaporators. Lignin as the available natural polymers possesses many advantages, such as hydrophilicity, biodegradability [42]. Due to its hydrophilicity, lignin could be cooperated into the aerogel-based solar evaporators for rapid water transportation. Out of weak hydrogen bonding between the lignin molecules, there were no reports about the lignin as the major component of aerogels for the solar steam generation. Cellulose as another abundant renewable polymers could be used as the bonding agent due to its rich hydroxyl group on the cellulose chains [43]. Although it is considered as a promising strategy to incorporate cellulose into lignin to fabricate aerogels, the inherent brittleness and poor mechanical strength of the biobased aerogels would limit their applications in the field of solar steam generation. So, it is a high demand on improving the mechanical properties of this type of aerogels and broadening its applications in the solar steam generation field.

To promote the solar steam generation efficiency, many researchers have been committed to the studies on the fabrication of the textures or arrays of the photothermal materials to reduce the light reflection. It is known that the light absorption ability is an important parameter to evaluate the performance of photothermal layers. According to the Fresnel equation, the light absorption ability of the photothermal layers is limited by the broadband light reflection due to their high refractive indices [44]. In the nature, plants and animals have evolved biological structures to absorb sunlight for keeping warm. These biological structures can improve the photothermal conversion performance by tailoring the absorption area and light multiple reflections. Such as the seedless sunflower [45,46] and the black scales of Bitis rhinoceros [47]. As we have known, the blackbody is a bulk or a surface on which energy of all photon is absorbed absolutely without reflection [45]. The topological structures of blackbody, such as cone-shaped, cellular and array structures could induce multiple light reflections to improve the photothermal performance [45]. Based on the multiple scattering effects inside the porous structure, the porous 3D-structure of the GO/melamine sponge was fabricated and the light absorption ability could reach up to 97.57% [18]. With a deployable, three-dimensional (3D) origami-based solar steam generator fabricated, the special structure with the periodic concavity pattern could recover radiative and convective heat loss efficiently for solar energy trapping [48]. In Nature, some plants show structural characteristics of trapping solar energy similar to blackbody. For an example, the 3D array blackbody-like structure of the seedless sunflower can induce sunlight multiple reflections to achieve the maximum heat energy [45,46]. With the special structure applied, the surficial light reflection of the photothermal materials would be minimized and the solar steam generation ability would be efficiently improved.

In this work, a novel spectrum-tailoring strategy was proposed for the proof-of-concept to narrow the bandgap of EGaIn using stearic acid (STA-EGaIn) through a green and facile mechanochemical approach for simultaneous improvement of the light absorption ability and the solar steam generation efficiency (**Scheme 1**). The stiff lignin was first introduced as preferred matrix of the aerogel scaffold and cellulose nanocrystal (CNC) was used as bonding agent of networks to prepare the lignin-CNC aerogel (LC aerogel) via freeze drying process. For the best use of the light absorption ability of STA-EGaIn, a double-layer solar evaporator of STA-EGaIn/lignin-CNC aerogel (SLC aerogel) was developed to improve the solar steam generation efficiency. Inspired by the seedless sunflower structurally, binary configurations of the topological SLC aerogel with the inverted pyramid topography (Inspired by the seedless sunflower) was for the first time engineered to reduce the multiple light reflection and enhance the energy-loss recovery for the



Scheme 1. Schematic illustration of fabrication of (a) STA-EGaIn, (b) SLC aerogel, IP-SLC aerogel.

excellent light-to-heat conversion performance of the lignin-based aerogel evaporator. The resulting IP-SLC aerogel will provide a range of promising applications, such as electronic sensors and the electricity generation. This work will open a new avenue to design a novel type of the photothermal coating layer with excellent light absorption ability for the efficient solar steam generation, sewage depuration and desalination, with wide applications of liquid metals in the electricity generation field ([Scheme 1](#)).

2. Result and discussions

2.1. Characterization of liquid metal and its derivatives

As shown in [Fig. 1\(a\)\(b\)](#), the liquid metal EGaIn exhibited the silver-colored and continuous liquid drop-like morphology, and the STA-EGaIn appeared black and powder morphology. Owing to the strong shearing force during the ball milling process, the spherical particles of EGaIn was turned to be powder like; The introduction of the stearic acid also changed the surface wettability and surface tension, making it disintegrated and thereby the powder morphology. It is known that the black color can absorb radiation from a broad section of the visible and near-infrared spectrum. With STA-EGaIn putting into the “solar”-

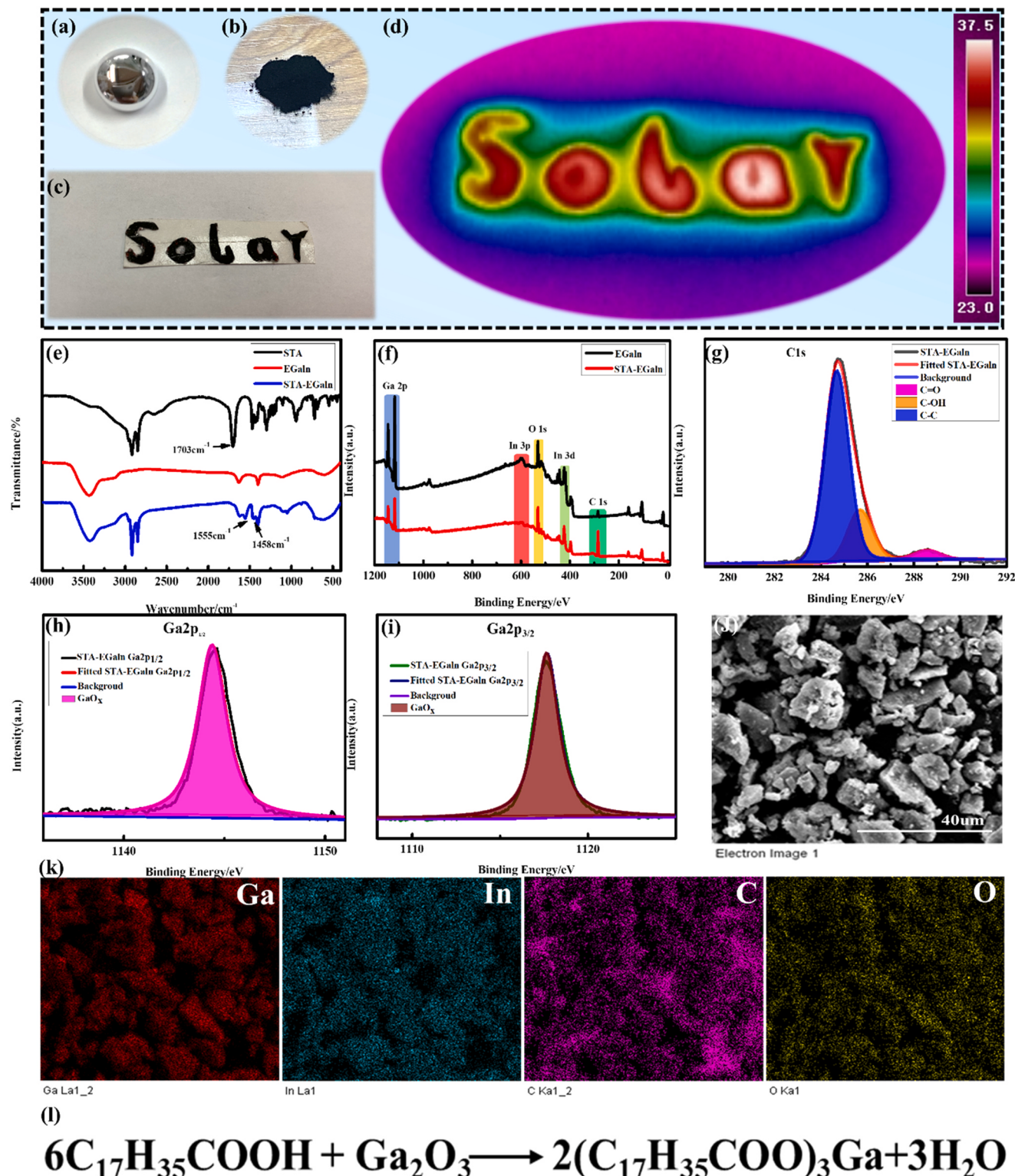


Fig. 1. (a)(b) Images of EGaIn and STA-EGaIn. (c) "Solar" morphology. (d) IR image of the "Solar" morphology. (e) FTIR curves of STA, EGaIn, and STA-EGaIn. (f) XPS curves of EGaIn and STA-EGaIn. (g) C 1s fitted XPS spectra of STA-EGaIn. (h)(i) Ga 2p fitted XPS spectra of STA-EGaIn. (j) SEM image of STA-EGaIn. (k) Mapping of STA-EGaIn. (l) Reaction equation of the EGaIn and STA.

lettered shape as shown in Fig. 1(c), the "solar" letters under the irradiation of 1 sun for 30 s showed the higher temperature as presented in Fig. 1(d) than the other locations, which proved the excellent photo-thermal conversion ability and rapid light response performance of STA-EGaIn. As shown in Fig. 1(e), STA-EGaIn showed new peaks at 2917 and 2848 cm⁻¹ in FTIR, which were attributed to the stretching vibration of

-CH₃ and -CH₂ groups of STA. New peaks at around 1555 and 1458 cm⁻¹ were attributed to the C=O band at 1555 cm⁻¹, indicating the formation of new chemical bond between EGaIn and STA. The disappearance of C=O in STA at 1703 cm⁻¹ proved the successful reaction between STA and EGaIn [49]. As showed in Fig. 1(g) in XPS measurement, the C=O and C-OH peaks from the C 1s peak indicated the favorable chemical

reaction between EGaIn and STA because carbon peak in EGaIn resulted from the adventitious carbon [50]. The two peaks of Ga 2p_{1/2} and Ga 2p_{3/2} in Fig. 1(h)(i) confirmed the existence of gallium oxide layer (Ga₂O or Ga₂O₃) [51]. As shown in Table S1, the increase in C content from 9.10% to 41.92% and the decrease in Ga content from 59.77% to 26.96% in STA-EGaIn proved the successful introduction of STA. Moreover, after ball milling, STA-EGaIn exhibited completely different morphology from EGaIn. As shown in SEM image of STA-EGaIn (Fig. 1(J)), STA-EGaIn with discontinuous irregular block-like shape morphology suggested the ball milling necessarily promoted the preferable chemical reaction between EGaIn and STA and changed its original morphology, while STA-EGaIn showed irregular block-like shape with the typical particle size of micrometers. The mapping images of STA-EGaIn in Fig. 1(k) showed that the C and O elements were uniformly distributed in the samples, indicating the homogeneous functionalization via mechanochemical treatment. With the EDX information of STA-EGaIn in Fig. S2, the increase of the C and O elements and

the decrease of the Ga and In elements in weight ratio in STA-EGaIn further confirmed the successful introduction of stearic acid and hence the preparation of STA-EGaIn. The ball milling of EGaIn with stearic acid, further facilitated the reaction between the -COOH of the SA and the Ga₂O₃ layer on the EGaIn surface. The reaction equation of EGaIn and stearic acid was given in Fig. 1(I).

2.2. Microstructures and mechanical robustness

The SLC and IP-SLC aerogels were fabricated through a directional freeze-drying process as shown in Fig. 2(a), with different surface morphologies of STA-EGaIn layer regulated by using different molds. During the ice-templating process, the ice crystals were grown vertically from the guidance of temperature-gradient at the bottom through the liquid nitrogen. The growth of ice crystals pushed the solutes in the solution mixture to the crystal boundaries, leading to the controllably self-assembling of lignin-CNC and PVA at the ice boundaries. The ice

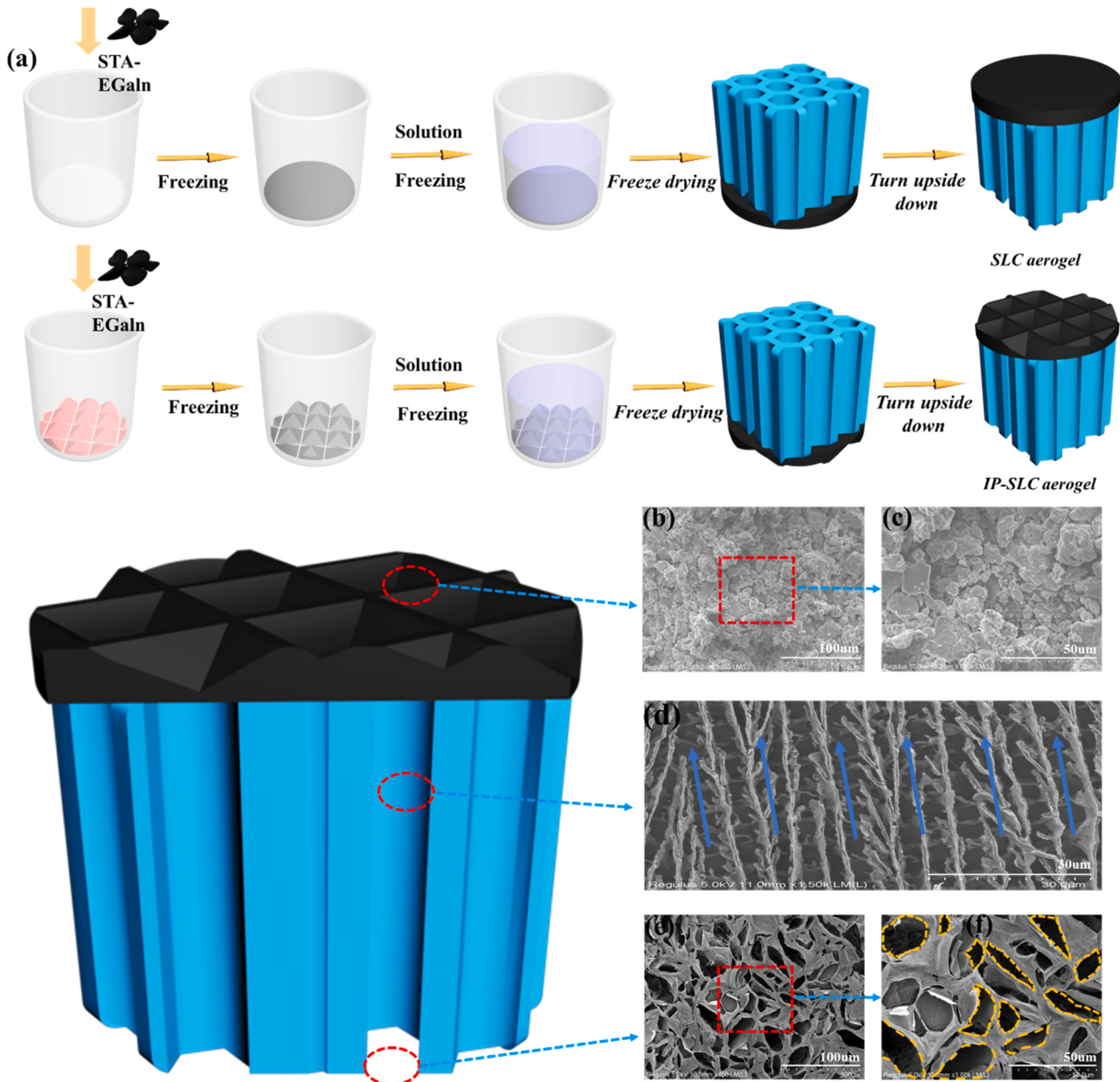


Fig. 2. (a) Fabrication of SLC and IP-SLC aerogels. (b-b₄) Illustration and SEM images showing the microstructure: (b) SEM image of top view. (c) Magnified SEM image of top view. (d) SEM image of interior side view. (e) SEM images of bottom view. (f) Magnified SEM image of bottom view.

growth finally drove bio-inspired honeycomb-like arrangement for surface topography, with the interior side view showing regularly patterned lamellar bridges of crumpled undulations for topology as shown in Fig. 2. The favorable binary microstructures enabled the preparation of a structure-stable and property-homogeneous lignin-aerogel. After sublimation of the ice crystals, the colloidal building blocks were synergistically coalesced and the resulted lignin-aerogel with well replicated ice crystal structures was obtained. From schematic diagram of IP-SLC aerogel in Fig. 2, and the SEM images of STA-EGaIn at top view, side view and bottom view in the Fig. 2(b-f), it could be found that the STA-EGaIn particles were seamlessly integrated with the surface of IP-SLC aerogel. The STA-EGaIn layer with a contact angle of 142° (Fig. 3(a)) was ascribed to the hydrophobicity of STA. To be noted, there was no apparent deformation after the water droplet completely lifted from the surface.

Closely related to the honeycomb-like and lamellar architectures as shown in Fig. 2(e) (f), the mechanical performance of IP-SLC aerogel was evaluated (Fig. 3(b)). With the stress applied, it was spread through the honeycomb-like pores walls and the compressed deformation of pores could facilitate to absorb the strain energy. Specifically, the compress stress at 40% strain of IP-SLC aerogel (49.3 kPa) was much higher than the previously reported works (as shown in Table S2). The 3D-architected porous structure endowed the engineered lignin-aerogel with structural stability and mechanical robustness, and low thermal conductivity for the better thermal harvesting management.

2.3. Solar steam generation

Solar steam generation is a promising method to produce pure water by capturing solar irradiation. As we know, the black color can absorb radiation from a broad section of the visible and near-infrared spectrum. Therefore, the STA-EGaIn microparticles (Fig. 1(b)) with excellent photothermal performance could be a good candidate for the solar steam generation optimization. To further improve the solar steam generation efficiency of LC aerogel, a bilayer-structured LC aerogel was fabricated as the basic building blocks with STA-EGaIn layer as the solar absorber. Two surface morphologies of the STA-EGaIn layers (flat and inverted-pyramid) were prepared to regulate the solar steam generation efficiency of the evaporators (Fig. 2(a)). The STA-EGaIn layer was uniformly coated on the LC aerogel surface with a contact angle of 142° (Fig. 3(a)). The hydrophobicity of the STA-EGaIn surface provided the preferable self-floating feature for the evaporator. With bio-inspired honeycomb-like pores and the regularly patterned lamellar bridges of crumpled undulations for topology of IP-SLC aerogel in Fig. 2(e)(f), open channels were formed for the fast water transport in the evaporation processes. Theoretically, the unbalanced wettability of the asymmetric

structures might allow the evaporator to float on water. Due to the hydrophilicity of CNC and lignin, SLC and IP-SLC aerogels could prefer to sink in the water and the hydrophilic side in the water could transfer water continuously. On the other hand, the hydrophobic layer of STA-EGaIn out of the water could efficiently absorb the solar energy. With the thermal conductivity of $0.07646 \text{ W m}^{-1} \text{ K}^{-1}$, the structured lignin-aerogel with low thermal conductivity could significantly minimize heat loss from the solar absorption layer to the water, and improve the solar steam generation efficiency. These advantages promised a great potential for the practical use of the developed evaporator in the solar steam generation.

It is known that light absorption ability is the key parameter of the solar steam generation performance. To better understand the light absorption ability of the as-prepared evaporators, the light absorption of the evaporators was measured by ultraviolet-visible (UV-vis) near-infrared (NIR) spectroscopy over wavelengths from 250 to 2500 nm. With the flat surface of SLC aerogel and the inverted-pyramid surface of IP-SLC aerogel as presented in Fig. 4(a)(b), IP-SLC aerogel presented lowest light reflectance, while SLC aerogel presented lower light reflectance than the LC aerogel as shown in Fig. 4(c). The exact values of light absorption from SLC aerogel and IP-SLC aerogel were 89.1% and 91%, respectively. Evidently, IP-SLC aerogel presented the better light absorption ability than the SLC aerogel over 250–2500 nm wavelengths (Fig. 4(d)). The higher light absorption ability originated from the multiple reflections of the inverted pyramid structure with length of 4.4 mm and a depth of 2.7 mm (Fig. 4(f)), indicating IP-SLC aerogel could capture the solar light more efficiently [50]. The light absorption ability of SLC and IP-SLC aerogels were higher than that of LC aerogel because of the excellent photothermal ability from the dense coating layer of STA-EGaIn (Fig. 4(c)). The temperature changes of the evaporation surface of water, SLC and IP-SLC aerogels under 1 sun irradiation over time could be used to evaluate photothermal characteristics of each evaporator. The infrared (IR) camera was used to record the surface temperature changes of each evaporator in the water under 1 sun irradiation. As shown in Fig. 4(e)(f), after being irradiated for 60 min, water and SLC aerogel showed uniform temperature distribution, with the surface temperatures up to 30.3 °C and 39.9 °C, respectively. The higher temperature of SLC aerogel was ascribed to the better light absorption ability. For IP-SLC aerogel in Fig. 4(g), the temperature in the V-shape spire of the inverted pyramid structure (40.9 °C) was higher than the top edge of the inverted pyramid structure (39.5 °C) because of the promoted multiple reflection of the diffuse light from the V-shape spire (Fig. 4(f)) and thus increased the light absorption ability.

The solar steam generation performance of the evaporators was investigated under the 1 kW m^{-2} illumination by measuring mass change of water in 60 min as presented in Fig. 5. As shown in Fig. 5(a),

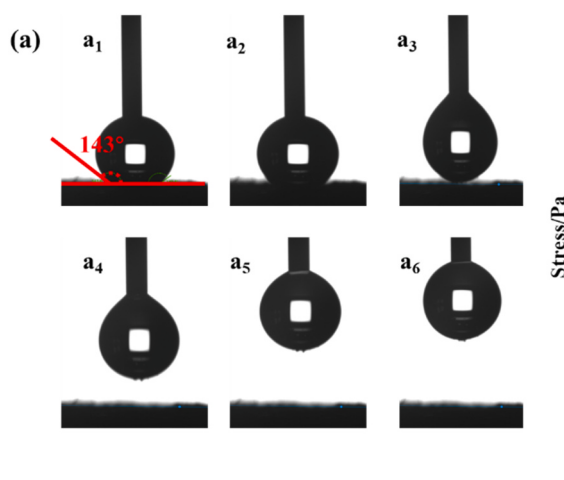


Fig. 3. (a) Optical image of the water dropped on the surface of STA-EGaIn surface. (b) Compressive property of IP-SLC aerogel.

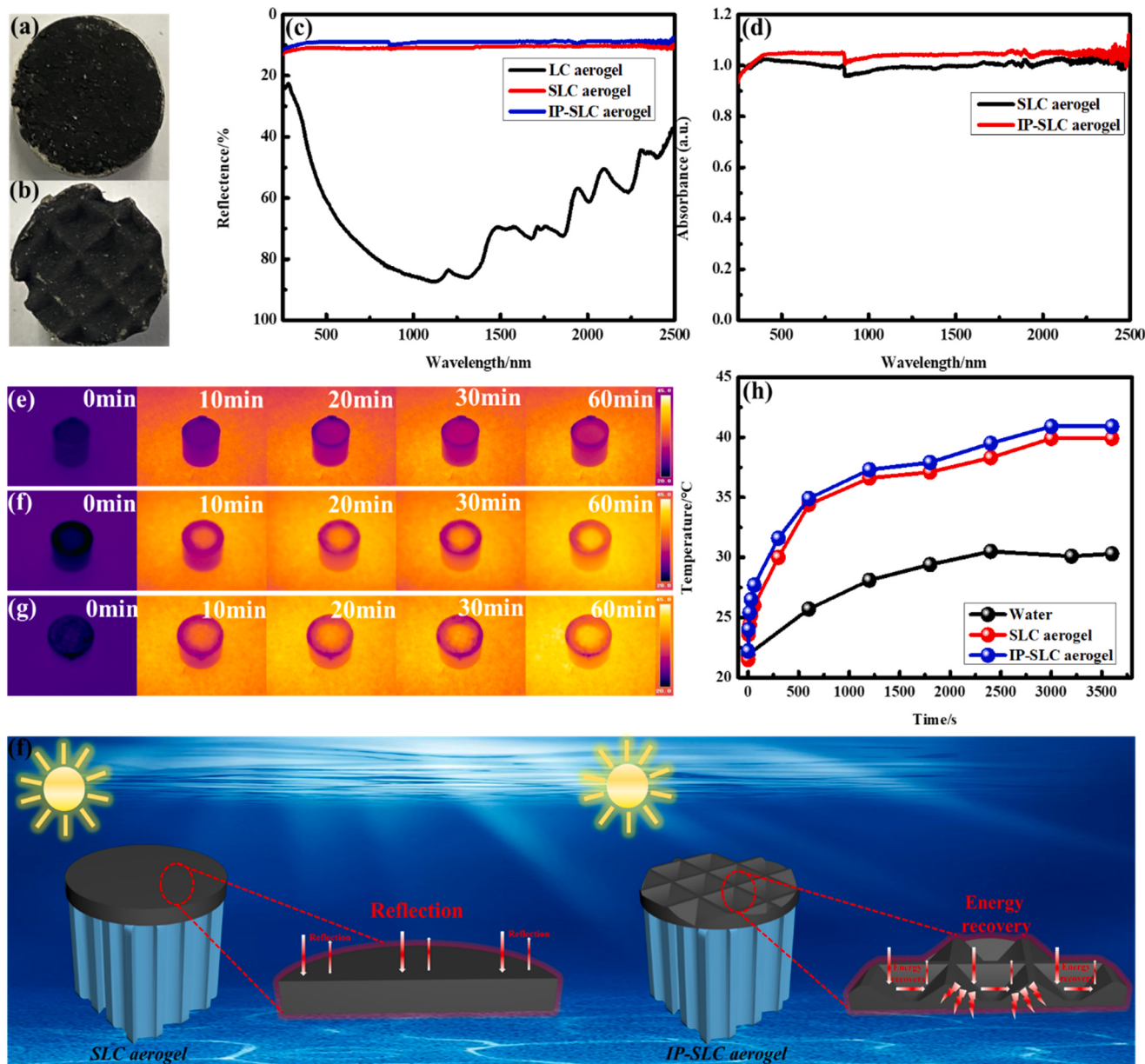


Fig. 4. (a)(b) Images of SLC and IP-SLC aerogels. (c) UV-vis-NIR reflection spectra of samples. (d) UV-vis-NIR absorbance spectra of the samples. (e)(f)(g) Infrared images demonstrated the temperature distribution of surface of water, SLC aerogel and IP-SLC aerogel under 1 sun at 0 min, 10 min, 20 min, 30 min, 60 min (h) Surface temperature evolution curves of water, SLC aerogel and IP-SLC aerogel under 1 sun irradiation during 1 h. (f) Schematic illustration of light reflection on the surfaces of SLC and IP-SLC aerogels.

during the solar steam generation process, the rough surface (the block-like morphology of STA-EGaIn) and the inverted pyramid topography of the STA-EGaIn layer could trigger multiple light reflections to reduce the reflection energy loss, then enhance the photothermal conversion performance of IP-SLC aerogel. Mass change of water with different evaporators was recorded under 1 kW m^{-2} illumination. As shown in Fig. 5(b), mass change of water was $\text{ca. } 0.56 \text{ kg m}^{-2} \text{ h}^{-1}$ after being irradiated for 1 h under 1 kW m^{-2} illumination. The low efficiency was mainly due to the low light absorption ability of water [52]. Under the same condition, with the addition of SLC and IP-SLC aerogels as photothermal evaporators, mass change of the evaporated water reached to 1.19 and $1.29 \text{ kg m}^{-2} \text{ h}^{-1}$, respectively. The remarkable enhancements were mainly attributed to the excellent light absorption ability of SLC and IP-SLC aerogels (Fig. 4(c)). The evaporation rate of IP-SLC system was 8.4% higher than SLC system. The results revealed that the IP-SLC evaporator with the inverted-pyramid structure could trigger multiple

light reflections to improve the light absorption ability. And it could also confine and recycle the convection and radiation heat within the walls to decrease the heat loss of surfaces. Finally, the evaporation performance could be enhanced [53].

The evaporation performance stability is also an important parameter for evaluating the evaporators. As shown in Fig. 5(d), the evaporation rate of IP-SLC system was relatively stable, indicating the structural reliability of IP-SLC aerogel. It could hence be suitable for the long-term solar steam generation. With the studies of the evaporation rate of IP-SLC aerogel under 1 sun irradiation for 1.5, 2 and 2.5 h, it was found that the average speed increased with the longer sunlight irradiation time (Fig. 5(e)). It was mainly ascribed to the IP-SLC aerogel required much time to reach stable state of evaporation rate, similar to the trend of temperature changes in Fig. 4(h). The longer the steady evaporation rate of IP-SLC aerogel maintained, the higher the average speed of IP-SLC aerogel became. With the sunlight irradiation time

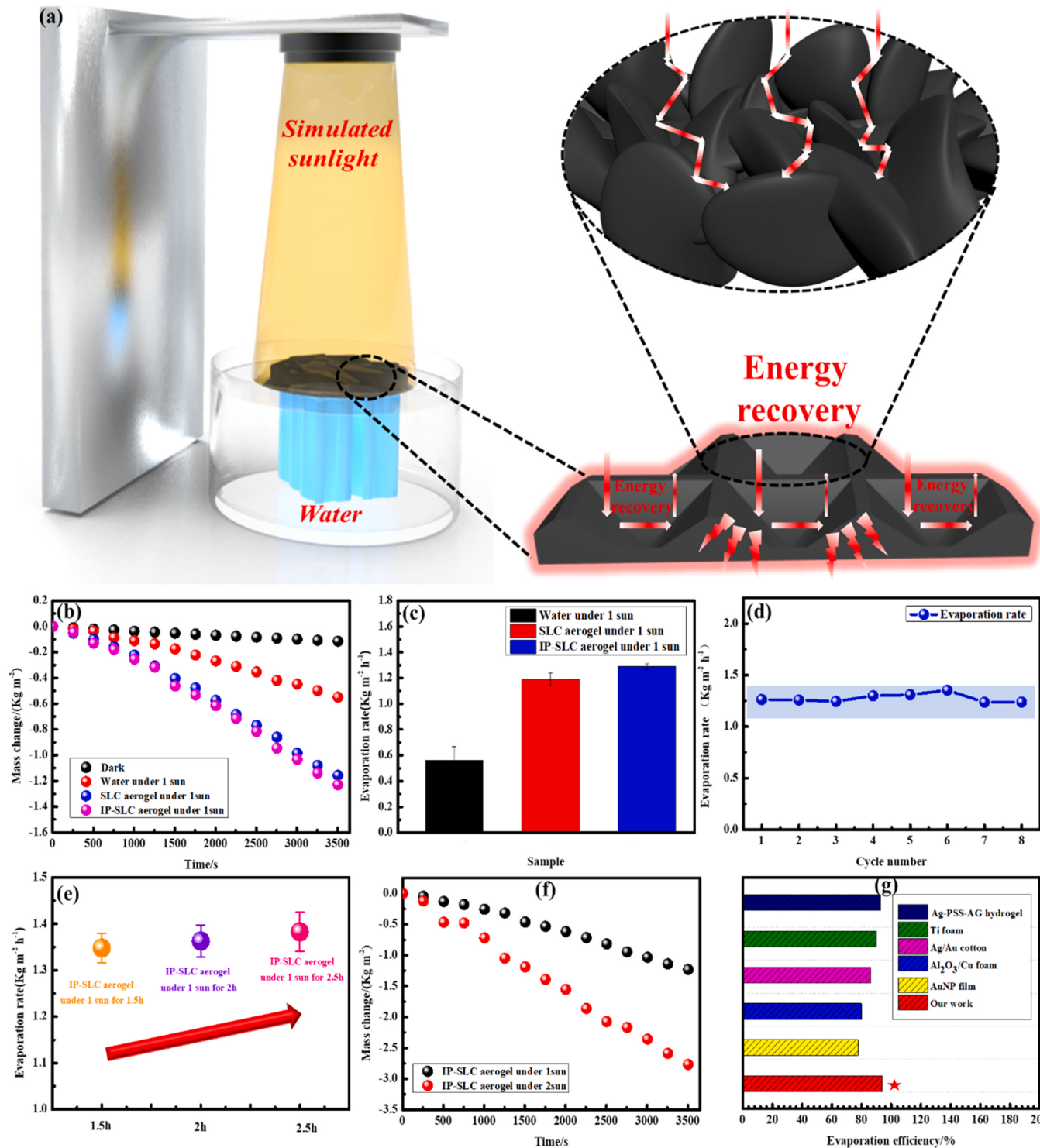


Fig. 5. (a) Schematic equipment of solar steam generation, and surface morphology of IP-SLC aerogel decreasing the reflection energy loss. (b) Mass change data for the different samples under different condition. (c) Evaporation rate data of water, SLC aerogel and IP-SLC aerogel under 1 sun irradiation. (d) Solar-driven water evaporation rate of IP-SLC aerogel for 8 cycles. (e) Evaporation rate data of IP-SLC aerogel under 1 sun irradiation for 1.5 h, 2 h, 2.5 h, respectively. (f) Mass change of IP-SLC aerogel under 1 and 2 sun irradiations. (g) Comparison of the evaporation efficiency with a series of solar steam generators: AuNP film ([56]), $\text{Al}_2\text{O}_3/\text{Cu}$ foam ([57]), Ag/Au cotton ([58]), Ti foam ([4]), Ag-PSS-AG hydrogel ([59]).

extended, the evaporation rate of IP-SLC aerogel could reach up to $1.38 \text{ kg m}^{-2} \text{ h}^{-1}$, 7% higher than its evaporation rate under 1 sun irradiation for 1 h. As shown in Fig. 5(f), the intensified sun irradiation could also induce higher evaporation rate, which was ascribed to the more sunlight heating [54].

The solar steam generation efficiency (η) is another parameter to

evaluate the solar steam generation performance. The efficiency could be calculated by the following equation:

$$\eta = \dot{m} * h_{LV} / q_i * C_{opt} \quad (1)$$

where \dot{m} is the mass flux while reaching steady state condition; h_{LV} is the

liquid-vapor phase enthalpy change containing sensible heat and phase change enthalpy; q_i is the solar irradiation power of 1 sun (1 kW m^{-2}); and C_{opt} is the optical concentration. The evaporation efficiency was calculated after 0.5 h sunlight irradiation when the evaporation rate was stable [55]. The solar steam generation efficiency of IP-SLC aerogel was *ca.* 94%, which could be comparably better than the results based on the metal based evaporators in the previously reported works (Fig. 5(g)) [4, 56–59]. These results suggested that the excellent solar steam generation performance of IP-SLC aerogel be achieved from the photothermal performance of STA-EGaIn and its binary configurations of interior topology and unique inverted pyramid topography. Practically, the cost of photothermal materials is important factor for the evaporator applications. The cost of STA-EGaIn and other kinds of photothermal materials were compared and shown in Table S3. The cost of the STA-EGaIn (0.35 \$/g) was relatively lower than that of most photothermal materials and possessed the promising potential for the practical applications. Therefore, the developed IP-SLC aerogel was evidently promising for the solar steam generation applications.

2.4. Photothermal promotion of STA-EGaIn

The photothermal mechanisms of STA-EGaIn for solar steam generation and harvesting were proposed in Fig. 6. Since EGaIn was easily oxidized in the air to form Ga_2O_3 layer on the surface, when EGaIn was

irradiated by the photons larger than the bandgap energy of Ga_2O_3 , the photons could be absorbed absolutely and converted into heat. However, the high bandgap energy hindered its photothermal performance and the EGaIn almost absorbed no solar energy at the visible wavelength. Therefore, it is particularly necessary to develop effective methods to tailor bandgap of EGaIn. In this work, STA-EGaIn was primarily prepared via a facile and green mechanochemical approach, *i.e.* ball milling. The as-prepared STA-EGaIn showed black color and excellent photothermal performance. As observed in Fig. 6, after EGaIn and STA-EGaIn were exposed to 1 sun irradiation for 1 h, surface temperature of EGaIn and STA-EGaIn could reach 27.9 °C and 56.7 °C, respectively. Comparing the bandgaps of EGaIn with STA-EGaIn (Fig. 6 (c)(d)), the bandgap of STA-EGaIn (0.24 eV) was definitely narrower than that of EGaIn (5.33 eV), which were derived from the T_{auc} equation [60]. As shown in the UPS curve (Fig. 6(e)), the highest occupied molecular orbital (HOMO) and the lowest unoccupied molecular orbital (LUMO) of STA-EGaIn was confirmed to be -9.10 and -8.86 eV, respectively. After the ball milling proceeded, EGaIn was further coated with STA. The negative hydrophilic radicals of STA would bind onto EGaIn surfaces to form a dipole layer. The dipole layer could induce an attracting potential to electrons inside EGaIn surfaces, and the bandgap of EGaIn could be finally reduced [30]. According to the photothermal conversion mechanisms of semiconductors, the most portion of the photons from the sunlight with higher energy than the bandgap of the

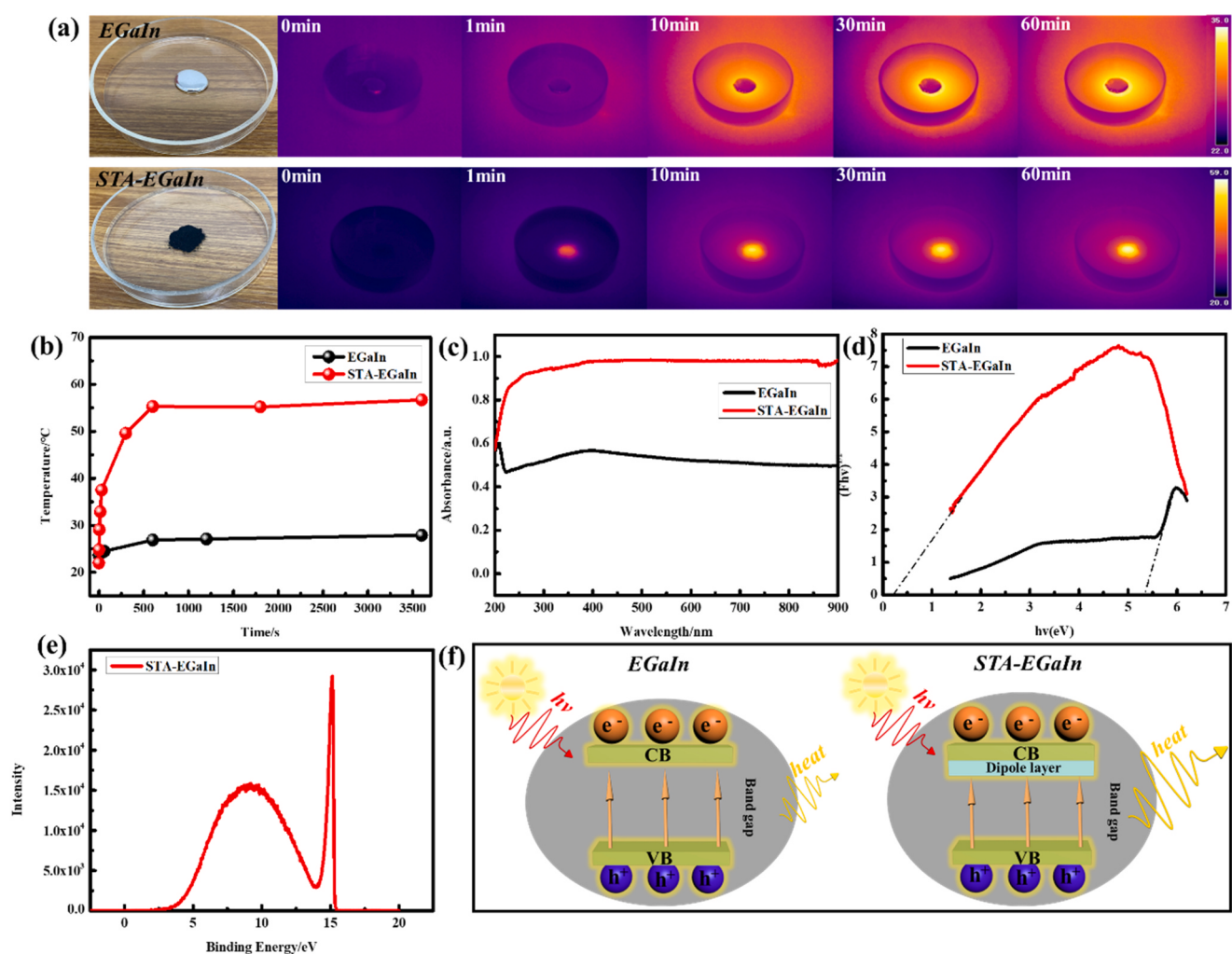


Fig. 6. (a) Infrared images of EGaIn and STA-EGaIn under 1 sun irradiation during 1 h. (b) Temperature evolution curves of EGaIn and STA-EGaIn during 1 h. (c) UV-vis absorption spectra of EGaIn and STA-EGaIn. (d) T_{auc} plots. (e) UPS curve of STA-EGaIn. (f) Schematic illustration of the band gap change of EGaIn and STA-EGaIn.

semiconductors will create above-bandgap electron-hole pairs in the semiconductors. The above-bandgap electrons and holes can relax to the band edges and convert the extra energy into heat by a thermalization process [61]. As shown in Fig. 6(f), under the same intensity of the sun irradiation, STA-EGaIn with narrow bandgap could convert more energy into heat than its counterpart, with less photons participated in the photothermal process. Therefore, STA-EGaIn showed excellent photothermal performance, promising great potential application in the fields of solar steam generation, desalination and electricity generation.

2.5. Multiphysics field simulation

To further understand heat transfer and water transport in IP-SLC aerogel, the COMSOL Multiphysics software was used to simulate temperature and pressure distributions of IP-SLC aerogel soaked in the water under 1 sun irradiation. As shown in the Fig. 7(a)(b), the 3D models with required size for SLC and IP-SLC aerogels were constructed in the finite element modeling. The temperature distributions of SLC and IP-SLC aerogels under 1 sun at 60 min were shown in Fig. 7(c)(d) and the temperature distribution of IP-SLC aerogel from 0 to 60 min were shown in Fig. S3. The higher surface temperature of the IP-SLC aerogel than the SLC aerogel could be ascribed to the evaporation from solar energy and the dissipation via radiation and convection [63]. From the relative water pressure distribution of IP-SLC aerogel (Fig. 7(e) and Fig. S4), it could be found that the higher value of the negative relative pressure at

the top side than the bottom side favorably ensured the continuous water transport for the solar steam generation. The water velocity distribution in IP-SLC aerogel clearly presented the efficient water transport to compensate the water loss on its surface during the solar steam generation process [62] as shown in Fig. 7(f) and Fig. S5. As shown in the Fig. 7(d) and Fig. S6, when surface temperature of IP-SLC aerogels was measured under 1 sun irradiation at 60 min, surface temperature of IP-SLC aerogel could reach approximately 41 °C, and both experimental measurements and simulated values showed similar temperature changes trend, thus indicating the correctness of the simulation model. The Fig. 7(g)(h) and Fig. 7(i)(j) were the surface temperature pictures from the simulation and the IR images of SLC and IP-SLC aerogels, respectively. From the IR images (Fig. 7(k)) of surface temperature distribution under 1 sun irradiation at 60 min as well as the relationship between surface temperature and irradiation time for IP-SLC aerogel, it could be found that temperature of the V-shape spire surface of IP-SLC aerogel was higher than its flat surface since the V-shape spire could promote the multiple reflection of the diffusing light to increase the light absorption ability. When the vapor diffuses from the bottom with high temperature (V-shape spire surface of IP-SLC aerogel) to the top with low temperature (Flat surface of IP-SLC aerogel), some heat from the water vapor molecules could favorably transfer to the cooler top (Flat surface of IP-SLC aerogel) via conduction, convection and radiation. Finally, the heat might be used for further evaporation process [63]. These results confirmed the promoted contribution of the dipole layer

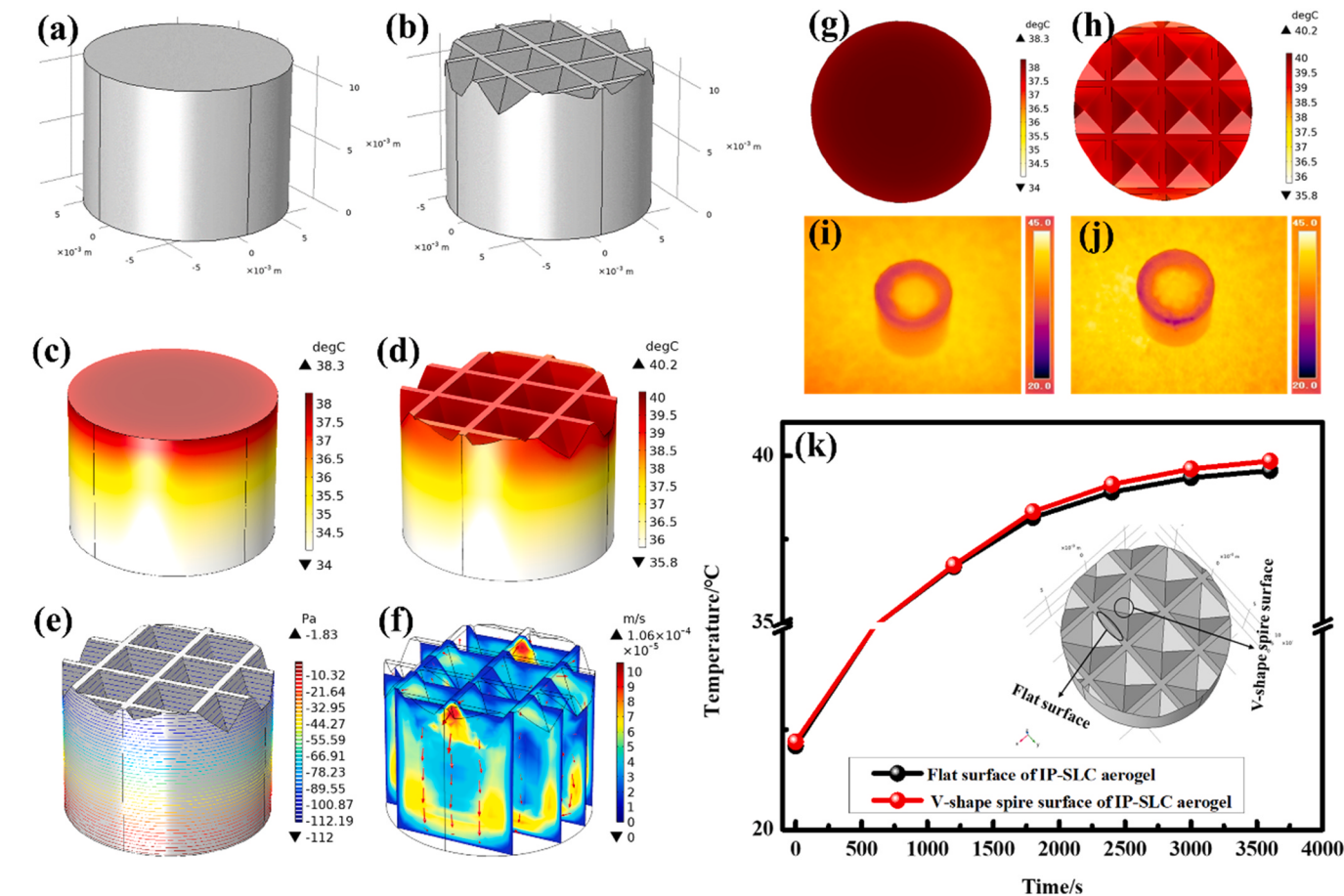


Fig. 7. Simulation of the solar steam generation of IP-SLC aerogel under 1 sun irradiation. (a)(b) Models of SLC and IP-SLC aerogels. (c) Temperature distribution of SLC aerogel under 1 sun irradiation at 60 min (d) Temperature distributions of IP-SLC aerogel surface under 1 sun irradiation at 60 min (e) Water pressure distributions of IP-SLC aerogel under 1 sun irradiation at 60 min (f) Water velocity distributions of IP-SLC aerogel under 1 sun irradiation at 60 min (g) Surface temperature distribution of SLC aerogel under 1 sun irradiation at 60 min (h) Surface temperature distribution of IP-SLC aerogel under 1 sun irradiation at 60 min (i) IR image of the temperature distribution of SLC aerogel under 1 sun irradiation at 60 min (j) IR image of temperature distribution of IP-SLC aerogel under 1 sun irradiation at 60 min (k) Temperature changes of the flat surface and V-shape spire surface of IP-SLC aerogel from 0 to 60 min.

and the V-shape spire surface topography for the excellent photothermal performance of STA-EGaIn in the water evaporation application of the entire system.

2.6. Seawater desalination and wastewater treatments

Solar energy is a sustainable and economic source that can be used for sewage and desalination treatments to produce fresh water [64,65]. As a promising aerogel material for efficient solar steam generation, the as-prepared IP-SLC aerogel can be used for sewage treatment. To evaluate the water purification property of IP-SLC aerogel, the experiment was carried out in the lab-scaled set-up *via* the solar steam generation process for solar steam collection (as shown in Fig. 8(a)). The rhodamine (RHB) solution (0.25 g/L, red color), seawater (Yellow sea, China) and the industry-sourced wastewater containing heavy metal ions *i.e.* Zn^{2+} , Ni^{2+} , Cu^{2+} , Fe^{3+} were employed as the water examples to be treated. As shown in Fig. 8(a), the IP-SLC aerogel could be floated on the wastewater surface in a container to absorb light and generate water vapor in a desiccator, then the water vapor condensed on the top of desiccator and collected from the petri dish. Experimental data of different water samples were illustrated in Fig. 8(b)(c)(d). Specifically, the color would be changed when the RHB contaminated water was purified to be fresh water. The removal of RHB could be also verified by UV-vis spectra, where the RHB contaminated water showed an obvious absorption in 554 nm and no peak could be observed after it was purified. To evaluate the desalination capability of IP-SLC aerogel, the seawater sample from

Yellow sea, China was used for demonstration. The salinity change after treatment could be tested by inductively coupled plasma optical emission spectrometry. The experimental results (shown in Fig. 8(c)) revealed that the salinity of Na^+ , Mg^{2+} , K^+ , Ca^{2+} in the seawater was significantly reduced after the treatment, with the ions rejection of 99% and the resultant salinity (Na^+ (2.06 mg/L), Mg^{2+} (0.046 mg/L), K^+ (0.114 mg/L), Ca^{2+} (0.09 mg/L)) of purified water could meet the drinking water standards [66]. The treatment of wastewater containing Zn^{2+} , Ni^{2+} , Cu^{2+} , Fe^{3+} was also performed using IP-SLC aerogel. It was obvious that the concentration of heavy metal ions of depurated water was dramatically reduced with the ion rejection of 99% after treatment. The IP-SLC aerogel could achieve the high removal efficiency for both organic pollutants and metal salts, indicating a promising potential to be applied in the solar-driven sewage and desalination treatments.

2.7. Electricity generation

Owing to the excellent photothermal property of STA-EGaIn, when the STA-EGaIn was operating on the surface of water, the temperature difference between STA-EGaIn and cold water appeared. Inspired by the temperature difference between STA-EGaIn and water, a PTE generator device with photo-thermal-electro performance was designed in the laboratory. The PTE device could generate electricity by the temperature difference between the two sides of PTE device due to the Seebeck effect [3,67,68]. As shown in Fig. 9(a), when the PTE device was supported by a sponge and floated on the water surface, the top side of PTE

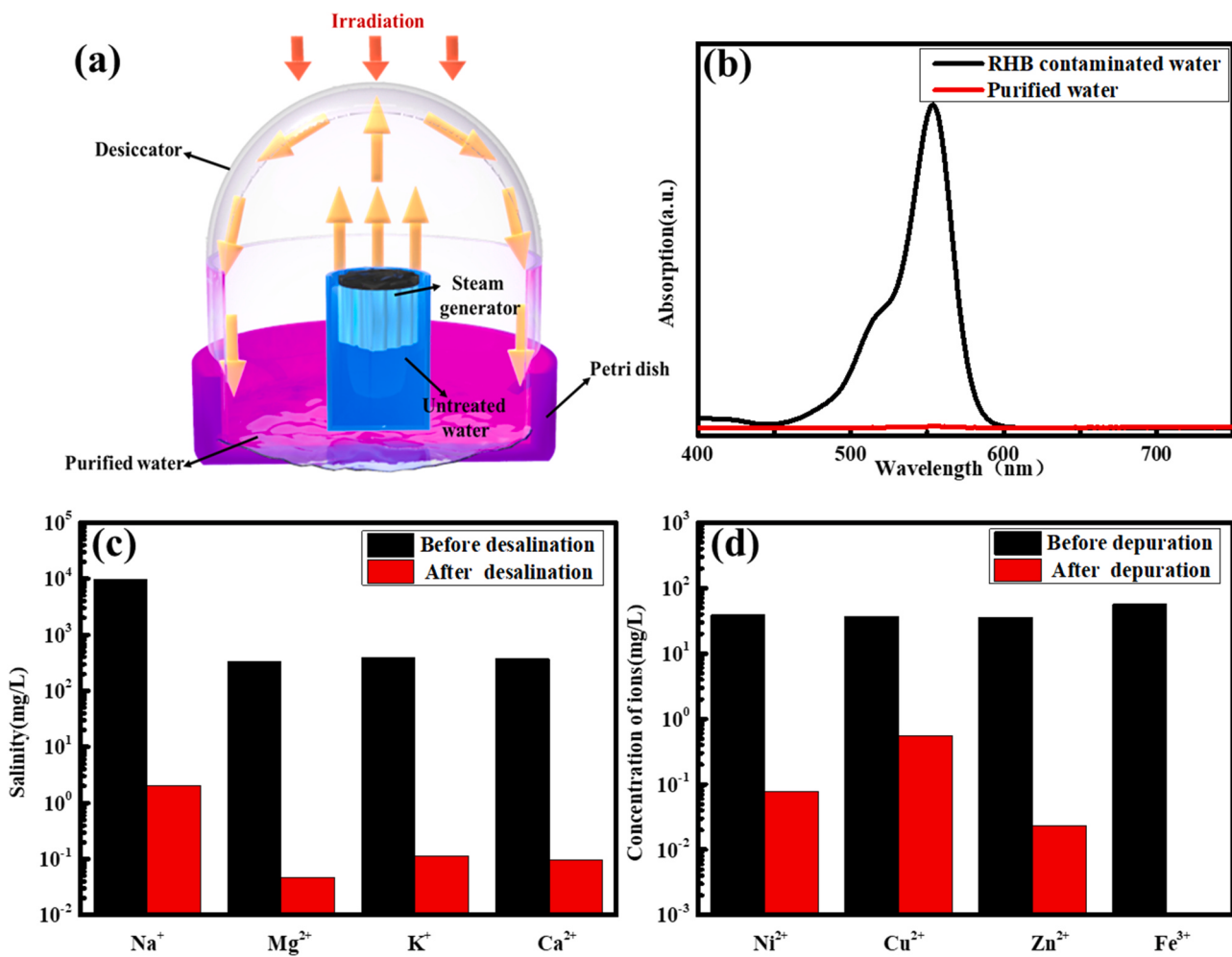


Fig. 8. (a) Scheme of lab-scaled set-up for solar steam collection of IP-SLC aerogel. (b) Absorption spectra of RHB contaminated water and condensed pure water. (c) Salinity values of metal ions in the seawater before and after treatment. (d) Concentrations of heavy-metal ions in the wastewater before and after the treatment.

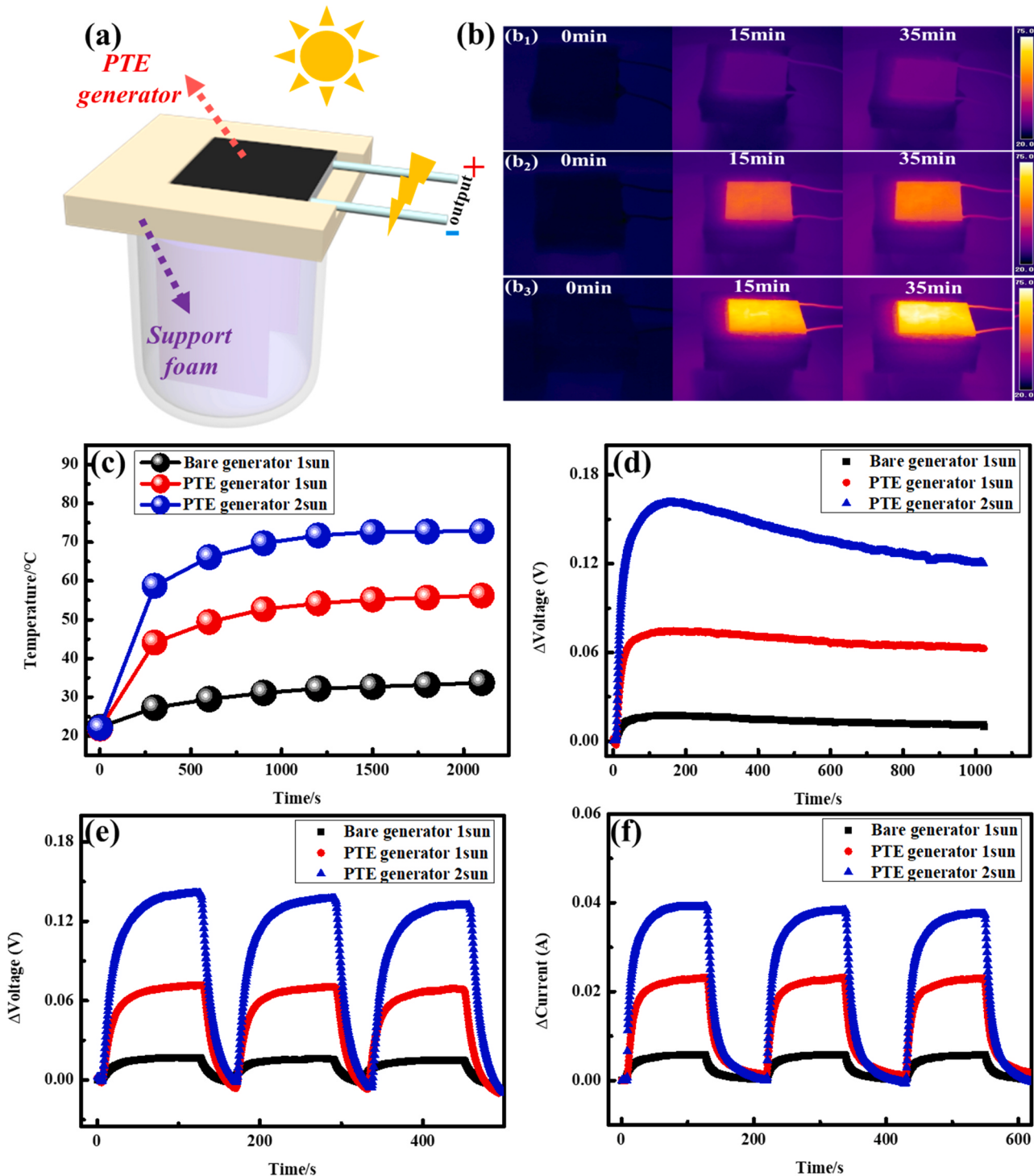


Fig. 9. (a) Digital image of PTE generator. (b) (b₁) Infrared image of surface temperature of the bare generator under 1 sun irradiation at 0, 15, 35 min; (b₂) Infrared image of surface temperature of PTE generator under 1 sun irradiation at 0, 15, 35 min; (b₃) Infrared image of surface temperature of the bare generator under 2 sun irradiation at 0, 15, 35 min (c) Surface temperature evolution curves of the bare generator, PTE generator under 1 sun irradiation, PTE generator under 2 sun irradiation. (d) Open-circuit voltage of the bare generator under 1 sun, the PTE generator under 1 and 2 sun. (e) Open-circuit voltage of the bare generator under 1 sun, PTE generator under 1 and 2 sun toward light cyclic responses. (f) Short-circuit current of the bare generator under 1 sun, PTE generator under 1 and 2 sun toward light cyclic responses.

device was carpeted with a layer of STA-EGaIn to create the high temperature side by absorbing solar energy, while the absorbent paper could draw the water up to the PTE device to create the cold side. When the PTE device was operating on the water surface, the open-circuit voltage (V_{oc}), short-circuit output current (I_{sc}) and current-voltage curves were recorded on an electrical workstation. Due to the excellent photothermal

property of STA-EGaIn, surface temperature of the PTE device (56.2 °C) at 35 min was higher than that of bare generator (33.7 °C) under 1 sun irradiation (in Fig. 9(b)(c)). When the irradiation was increased from 1 sun to 2 sun, surface temperature of the PTE device at 35 min increased to 72.8 °C, being consistent with surface temperature response in Fig. 4(h). Under 1 sun irradiation, the bare generator could produce a

maximum voltage output of 17.56 mV (Fig. 9(d)). The PTE device could produce a maximum voltage output of 74.43 and 161.13 mV at irradiations of 1 sun and 2 sun, respectively. The maximum output voltage of the PTE device under 1 sun irradiation was higher than that of the bare generator owing to the distinguished photo-thermal property of STA-EGaIn. However, the output voltages (1 sun and 2 sun) presented decreasing trend after reaching maximum and kept stable state after 600 s, which ultimately reflected the transfer gradient change in the solar energy for the photo-thermo-electrical conversion. The phenomenon was consistent with the previous reports from the other groups [54, 69]. Switching on the light by three on-off cycles, as shown in the Fig. 9 (e)(f), the PTE device generated the output open-circuit voltage and the short-circuit current. The short-circuit output current values of the bare generator at 1 sun irradiation and the PTE generator at 1 sun and 2 sun irradiations were 5.77, 23.09 and 39.15 mA, respectively. The short-circuit output current toward cyclic response of light exhibited the similar trend to the open-circuit output voltage, with stable photo-thermal-electro generation. Above all, STA-EGaIn could be a promising material in the photo-thermo-electrical field.

3. Conclusion

In summary, a novel photothermal liquid metal with the tailored spectrum was successfully prepared via the dipole layer strategy for highly efficient solar steam generation through a green and facile mechanochemical approach. For the proof-of-concept, the blackbody-inspired lignin-aerogel with the spectrum-tailored gallium and indium alloy achieved solar steam generation efficiency up to 94% based on the energy-loss recovery and the strong absorptivity of dipole layers. Inspired by seedless sunflower structurally, the liquid metal-configured layer with inverted pyramid topography was applied as a highly efficient light absorber and the desirable self-floating regulator. Furthermore, the architectured binary configurations of interior topology and surface topography for the layer-doubled lignin-aerogel greatly contributed to the superior mechanical strength (49.3 kPa at 50% strain), extraordinary light absorption efficiency (*ca.* 94%) and rapid water transportation for the fresh water generation through synergistic mechanisms of structured multiple light reflection and sunflower-inspired blackbody. In addition to these favorable properties, the resulted lignin-aerogel showed a great potential in reducing the ion concentration in seawater and sewage with the removal efficiency up to 99% and the practical applications in the field of electricity generation. This work will provide a promising and versatile strategy to improve the light absorption ability of liquid metals for efficient solar steam generation of the layer-doubled aerogels in the applications of solar-driven water purification, solar steam and electricity generation.

CRediT authorship contribution statement

Wei Zechang: Data curation, Writing- Original draft preparation. **Cai Chenyang:** Methodology, Writing- Reviewing. **Huang Yangze:** Investigation, Writing- Reviewing. **Wang Yongqin:** Investigation, Visualization. **Fu Yu:** Conceptualization, Supervision, Writing- Reviewing and Editing.

Declaration of Competing Interest

The authors declare that they have no known competing financial interests or personal relationships that could have appeared to influence the work reported in this paper.

Acknowledgments

The work at Nanjing Forestry University was supported by the National Natural Science Foundation of China (Grant No. 31770608), Jiangsu Specially-appointed Professorship Program (Sujiaoshi [2016]

20), Science and Technology Innovation Project for Overseas Students of Nanjing City (Ningrenshehan [2018]214), the Postgraduate Research & Practice Innovation Program of Jiangsu Province [Grant No. KYCX19_1087], and Analytical and Testing Assistance from Analysis and Test Center of Nanjing Forestry University.

Appendix A. Supporting information

Supplementary data associated with this article can be found in the online version at doi:10.1016/j.nanoen.2021.106138.

References

- [1] X.-Y. Wang, J. Xue, C. Ma, T. He, H. Qian, B. Wang, J. Liu, Y. Lu, Anti-biofouling double-layered unidirectional scaffold for long-term solar-driven water evaporation, *J. Mater. Chem. A* 7 (2019) 16696–16703.
- [2] J. Chen, J. Feng, Z. Li, P. Xu, X. Wang, W. Yin, M. Wang, X. Ge, Y. Yin, Space-confined seeded growth of black silver nanostructures for solar steam generation, *Nano Lett.* 19 (2019) 400–407.
- [3] Z. Zheng, H. Li, X. Zhang, H. Jiang, X. Geng, S. Li, H. Tu, X. Cheng, P. Yang, Y. Wan, High-absorption solar steam device comprising Au@Bi₂MoO₆-CDs: extraordinary desalination and electricity generation, *Nano Energy* 68 (2020), 104298.
- [4] K. Yin, S. Yang, J. Wu, Y. Li, D. Chu, J. He, J.-A. Duan, Femtosecond laser induced robust Ti foam based evaporator for efficient solar desalination, *J. Mater. Chem. A* 7 (2019) 8361–8367.
- [5] K. Yin, S. Yang, X. Dong, D. Chu, J.-A. Duan, J. He, Ultrafast achievement of a superhydrophilic/hydrophobic janus foam by femtosecond laser ablation for directional water transport and efficient fog harvesting, *ACS Appl. Mater. Interfaces* 10 (2018) 31433–31440.
- [6] J. Liu, Q. Liu, D. Ma, Y. Yuan, J. Yao, W. Zhang, H. Su, Y. Su, J. Gu, D. Zhang, Simultaneously achieving thermal insulation and rapid water transport in sugarcane stems for efficient solar steam generation, *J. Mater. Chem. A* 7 (2019) 9034–9039.
- [7] B.P. Chaplin, Critical review of electrochemical advanced oxidation processes for water treatment applications, *Environ. Sci. Process. Impacts* 16 (2014) 1182–1203.
- [8] F. Jiang, H. Liu, Y. Li, Y. Kuang, X. Xu, C. Chen, H. Huang, C. Jia, X. Zhao, E. Hitz, Y. Zhou, R. Yang, L. Cui, L. Hu, Lightweight, mesoporous, and highly absorptive all-anofiber aerogel for efficient solar steam generation, *ACS Appl. Mater. Interfaces* 10 (2018) 1104–1112.
- [9] Y. Guo, H. Lu, F. Zhao, X. Zhou, W. Shi, G. Yu, Biomass-derived hybrid hydrogel evaporators for cost-effective solar water purification, *Adv. Mater.* 32 (2020), 1907061.
- [10] Y. Zhou, T. Ding, M. Gao, K.H. Chan, Y. Cheng, J. He, G.W. Ho, Controlled heterogeneous water distribution and evaporation towards enhanced photothermal water-electricity-hydrogen production, *Nano Energy* 77 (2020), 105102.
- [11] F.L. Meng, M. Gao, T. Ding, G. Yilmaz, W.L. Ong, G.W. Ho, Modular deformable steam electricity cogeneration system with photothermal, water, and electrochemical tunable multilayers, *Adv. Funct. Mater.* 30 (2020), 2002867.
- [12] Z. Yin, H. Wang, M. Jian, Y. Li, K. Xia, M. Zhang, C. Wang, Q. Wang, M. Ma, Q.-S. Zheng, Y. Zhang, Extremely black vertically aligned carbon nanotube arrays for solar steam generation, *ACS Appl. Mater. Interfaces* 9 (2017) 28596–28603.
- [13] A. Guo, X. Ming, Y. Fu, G. Wang, X. Wang, Fiber-based, double-sided, reduced graphene oxide films for efficient solar vapor generation, *ACS Appl. Mater. Interfaces* 9 (2017) 29958–29964.
- [14] M. Zhu, Y. Li, F. Chen, X. Zhu, J. Dai, Y. Li, Z. Yang, X. Yan, J. Song, Y. Wang, E. Hitz, W. Luo, M. Lu, B. Yang, L. Hu, Plasmonic wood for high-efficiency solar steam generation, *Adv. Energy Mater.* 8 (2018), 1701028.
- [15] K. Bae, G. Kang, S.K. Cho, W. Park, K. Kim, W.J. Padilla, Flexible thin-film black gold membranes with ultrabroadband plasmonic nanofocusing for efficient solar vapour generation, *Nat. Commun.* 6 (2015) 10103.
- [16] F. Tao, Y. Zhang, K. Yin, S. Cao, X. Chang, Y. Lei, D.s Wang, R. Fan, L. Dong, Y. Yin, X. Chen, *ACS Appl. Mater. Interfaces* (2018) 35154–35163.
- [17] M. Shang, N. Li, S. Zhang, T. Zhao, C. Zhang, C. Liu, H. Li, Z. Wang, Extracellular volume fraction measurements derived from the longitudinal relaxation of blood-based synthetic hematocrit may lead to clinical errors in 3 T cardiovascular magnetic resonance, *J. Cardiovasc. Magn. Reson.* 20 (2018) 56–61.
- [18] B. Huo, D. Jiang, X. Cao, H. Liang, Z. Liu, C. Li, J. Liu, N-doped graphene /carbon hybrid aerogels for efficient solar steam generation, *Carbon* 142 (2019) 13–19.
- [19] Y. Long, S. Huang, H. Yi, J. Chen, J. Wu, Q. Liao, H. Liang, H. Cui, S. Ruan, Y.-J. Zeng, Carrot-inspired solar thermal evaporator, *J. Mater. Chem. A* 7 (2019) 26911–26916.
- [20] X. Zhang, X. Wang, W.D. Wu, X.D. Chen, Z. Wu, Self-floating monodisperse microparticles with a nano-engineered surface composition and structure for highly efficient solar-driven water evaporation, *J. Mater. Chem. A* 7 (2019) 6963–6971.
- [21] M. Wang, P. Wang, J. Zhang, C. Li, Y. Jin, A ternary Pt/Au/TiO₂ -decorated plasmonic wood carbon for high-efficiency interfacial solar steam generation and photodegradation of tetracycline, *ChemSusChem* 12 (2019) 467–472.
- [22] M.S. Zieliński, J.-W. Choi, T. La Grange, M. Modestino, S.M.H. Hashemi, Y. Pu, S. Birkhold, J.A. Hubbell, D. Psaltis, Hollow mesoporous plasmonic nanoshells for enhanced solar vapor generation, *Nano Lett.* 16 (2016) 2159–2167.

- [23] S. Cao, Q. Jiang, X. Wu, D. Ghim, H. Gholami Derami, P.-I. Chou, Y.-S. Jun, S. Singamaneni, Advances in solar evaporator materials for freshwater generation, *J. Mater. Chem. A* 7 (2019) 24092–24123.
- [24] P. Ying, M. Li, F. Yu, Y. Geng, L. Zhang, J. He, Y. Zheng, R. Chen, Band gap engineering in an efficient solar-driven interfacial evaporation system, *ACS Appl. Mater. Interfaces* 12 (2020) 32880–32887.
- [25] X. Zhang, G. Wu, X.-C. Yang, MoS₂nanosheet–carbon foam composites for solar steam generation, *ACS Appl. Nano Mater.* 3 (2020) 9706–9714.
- [26] Y. Lin, C. Cooper, M. Wang, J.J. Adams, J. Genzer, M.D. Dickey, Handwritten, soft circuit boards and antennas using liquid metal nanoparticles, *Small* 11 (2015) 6397–6403.
- [27] L. Ren, J. Zhuang, G. Casillas, H. Feng, Y. Liu, X. Xu, Y. Liu, J. Chen, Y. Du, L. Jiang, S.X. Dou, Nanodroplets for stretchable superconducting circuits, *Adv. Funct. Mater.* 26 (2016) 8111–8118.
- [28] S.A. Chechetka, Y. Yu, X. Zhen, M. Pramanik, K. Pu, E. Miyako, Light-driven liquid metal nanotransformers for biomedical theranostics, *Nat. Commun.* 8 (2017) 15432.
- [29] Y. Xin, H. Peng, J. Xu, J. Zhang, Ultrauniform embedded liquid metal in sulfur polymers for recyclable, conductive, and self-healable materials, *Adv. Funct. Mater.* 29 (2019) 1808989.
- [30] B. Zhou, L. Xiao, T.J. Li, J. Zhao, Z. Lai, S. Gu, Absorption redshift in TiO₂ultrafine particles with surfacial dipole layer, *Appl. Phys. Lett.* 59 (1991) 1826–1828.
- [31] T. Ding, Y. Zhou, W.L. Ong, G.W. Ho, Second-order bipartite consensus for networked robotic systems with quantized-data interactions and time-varying transmission delays, *ISA Trans.* 108 (2021) 178–187.
- [32] P. Tao, G. Ni, C. Song, W. Shang, J. Wu, J. Zhu, G. Chen, T. Deng, Solar-driven interfacial evaporation, *Nat. Energy* 3 (2018) 1031–1041.
- [33] G. Xue, K. Liu, Q. Chen, P. Yang, J. Li, T. Ding, J. Duan, B. Qi, J. Zhou, Robust and low-cost flame-treated wood for high-performance solar steam generation, *ACS Appl. Mater. Interfaces* 9 (2017) 15052–15057.
- [34] G. Wang, Y. Fu, A. Guo, T. Mei, J. Wang, J. Li, X. Wang, TTE DNA-Gu NPs: enhanced fluorescence and application in a target DNA triggered dual-cycle amplification biosensor, *Chem. Commun.* 53 (2017) 5629–5632.
- [35] F. Zhang, Y. Li, X. Bai, S. Wang, B. Liang, G. Fu, Z.-S. Wu, Synthesis of mesoporous Fe3Si aerogel as a photo-thermal material for highly efficient and stable corrosive-water evaporation, *J. Mater. Chem. A* 6 (2018) 23263–23269.
- [36] Y. Fu, G. Wang, X. Ming, X. Liu, B. Hou, T. Mei, J. Li, J. Wang, X. Wang, Association between toll-like receptor 4 T399I gene polymorphism and the susceptibility to crohn's disease: a meta-analysis of case-control studies, *Digestion* 97 (2018) 250–259.
- [37] C. Cai, Z. Wei, Y. Huang, C. Ding, P. Wang, J. Song, L. Deng, Y. Fu, W.H. Zhong, Ultralight programmable bioinspired aerogels with an integrated multifunctional surface for self-cleaning, oil absorption, and thermal insulation via coassembly, *ACS Appl. Mater. Interfaces* 12 (2020) 11273–11286.
- [38] M. Tan, J. Wang, W. Song, J. Fang, X. Zhang, Self-floating hybrid hydrogels assembled with conducting polymer hollow spheres and silica aerogel microparticles for solar steam generation, *J. Mater. Chem. A* 7 (2019) 1244–1251.
- [39] P. Mu, W. Bai, Z. Zhang, J. He, H. Sun, Z. Zhu, W. Liang, A. Li, Robust aerogels based on conjugated microporous polymer nanotubes with exceptional mechanical strength for efficient solar steam generation, *J. Mater. Chem. A* 6 (2018) 18183–18190.
- [40] P. Mu, Z. Zhang, W. Bai, J. He, H. Sun, Z. Zhu, W. Liang, A. Li, Superwetting monolithic hollow-carbon-nanotubes aerogels with hierarchically nanoporous structure for efficient solar steam generation, *Adv. Energy Mater.* 9 (2019), 1802158.
- [41] L. Yang, G. Chen, N. Zhang, Y. Xu, X. Xu, Sustainable biochar-based solar absorbers for high-performance solar-driven steam generation and water purification, *ACS Sustain. Chem. Eng.* 7 (2019) 19311–19320.
- [42] C. Wang, Y. Xiong, B. Fan, Q. Yao, H. Wang, C. Jin, Q. Sun, Cellulose as an adhesion agent for the synthesis of lignin aerogel with strong mechanical performance, Sound-absorption and thermal Insulation, *Sci. Rep.* 6 (2016) 32383.
- [43] A.C. O'Sullivan, Thankfully the era of ranitidine for every woman in labour has passed, *Int. J. Obstet. Anesth.* 6 (1997), 173–5.
- [44] K. Li, T.-H. Chang, Z. Li, H. Yang, F. Fu, T. Li, J.S. Ho, P.-Y. Chen, Biomimetic MXene textures with enhanced light-to-heat conversion for solar steam generation and wearable thermal management, *Adv. Energy Mater.* 9 (2019), 1901687.
- [45] Y. Chen, G. Zhao, L. Ren, H. Yang, X. Xiao, W. Xu, Blackbody-Inspired array structural polypyrrole-sunflower disc with extremely high light absorption for efficient photothermal evaporation, *ACS Appl. Mater. Interfaces* 12 (2020) 46653–46660.
- [46] P. Sun, W. Zhang, I. Zada, Y. Zhang, J. Gu, Q. Liu, H. Su, D. Pantelić, B. Jelenković, D. Zhang, 3D-structured carbonized sunflower heads for improved energy efficiency in solar steam generation, *ACS Appl. Mater. Interfaces* 12 (2020) 2171–2179.
- [47] K. Li, T.-H. Chang, Z. Li, H. Yang, F. Fu, T. Li, J.S. Ho, P.-Y. Chen, Biomimetic MXene textures with enhanced light-to-heat conversion for solar steam generation and wearable thermal management, *Adv. Energy Mater.* 9 (2019), 1901687.
- [48] S. Hong, Y. Shi, R. Li, C. Zhang, Y. Jin, P. Wang, Nature-inspired, 3D origami solar steam generator toward near full utilization of solar energy, *ACS Appl. Mater. Interfaces* 10 (2018) 28517–28524.
- [49] Y. Si, Z. Guo, W. Liu, A robust epoxy resins @ stearic acid-Mg(OH)₂ micronanosheet superhydrophobic omnipotent protective coating for real-life applications, *ACS Appl. Mater. Interfaces* 8 (2016) 16511–16520.
- [50] A.R. Jacob, D.P. Parekh, M.D. Dickey, L.C. Hsiao, Interfacial rheology of gallium-based liquid metals, *Langmuir* 35 (2019) 11774–11783.
- [51] Z. Chen, J.B. Lee, Surface modification with gallium coating as nonwetting surfaces for gallium-based liquid metal droplet manipulation, *ACS Appl. Mater. Interfaces* 11 (2019) 35488–35495.
- [52] Q. Yang, C. Xu, F. Wang, Z. Ling, Z. Zhang, X. Fang, A high-efficiency and low-cost interfacial evaporation system based on graphene-loaded pyramid polyurethane sponge for wastewater and seawater treatments, *ACS Appl. Energy Mater.* 2 (2019) 7223–7232.
- [53] Y. Zhang, T. Xiong, D.K. Nandakumar, S.C. Tan, Structure architecting for salt-rejecting solar interfacial desalination to achieve high-performance evaporation with in situ energy generation, *Adv. Sci.* 7 (2020), 1903478.
- [54] H. Jiang, L. Ai, M. Chen, J. Jiang, Insight into the deep eutectic solvent extraction mechanism of flavonoids from natural plant, *ACS Sustain. Chem. Eng.* 8 (2020) 19169–19177.
- [55] X.-J. Zha, X. Zhao, J.-H. Pu, L.-S. Tang, K. Ke, R.-Y. Bao, L. Bai, Z.-Y. Liu, M.-B. Yang, W. Yang, Flexible anti-biofouling mxene/cellulose fibrous membrane for sustainable solar-driven water purification, *ACS Appl. Mater. Interfaces* 11 (2019) 36589–36597.
- [56] Y. Liu, S. Yu, R. Feng, A. Bernard, Y. Liu, Y. Zhang, H. Duan, W. Shang, P. Tao, C. Song, T. Deng, A bioinspired, reusable, paper-based system for high-performance large-scale evaporation, *Adv. Mater.* 27 (2015) 2768–2774.
- [57] N. Xu, J. Li, Y. Wang, C. Fang, X. Li, Y. Wang, L. Zhou, B. Zhu, Z. Wu, S. Zhu, J. Zhu, A water lily-inspired hierarchical design for stable and efficient solar evaporation of high-salinity brine, *Sci. Adv.* 5 (2019) 7013.
- [58] H.D. Kiriarachchi, F.S. Awad, A.A. Hassan, J.A. Bobb, A. Lin, M.S. El-Shall, Plasmonic chemically modified cotton nanocomposite fibers for efficient solar water desalination and wastewater treatment, *Nanoscale* 10 (2018) 18531–18539.
- [59] Z. Sun, J. Wang, Q. Wu, Z. Wang, Z. Wang, J. Sun, C.-J. Liu, Plasmon based double-layer hydrogel device for a highly efficient solar vapor generation, *Adv. Funct. Mater.* 29 (2019), 1901312.
- [60] X. Chen, C. Meng, Y. Wang, Q. Zhao, Y. Li, X.-M. Chen, D. Yang, Y. Li, Y. Zhou, Laser-synthesized rutile TiO₂with abundant oxygen vacancies for enhanced solar water evaporation, *ACS Sustain. Chem. Eng.* 8 (2020) 1095–1101.
- [61] G. Liu, J. Xu, K. Wang, Solar water evaporation by black photothermal sheets, *Nano Energy* 41 (2017) 269–284.
- [62] H. Wang, R. Zhang, D. Yuan, S. Xu, L. Wang, Gas foaming guided fabrication of 3D porous plasmonic nanoplatform with broadband absorption, tunable shape, excellent stability, and high photothermal efficiency for solar water purification, *Adv. Funct. Mater.* 30 (2020), 2003995.
- [63] S. Hong, Y. Shi, R. Li, C. Zhang, Y. Jin, P. Wang, Nature-inspired, 3D origami solar steam generator toward near full utilization of solar energy, *ACS Appl. Mater. Interfaces* 10 (2018) 28517–28524.
- [64] Y. Zhang, H. Zhang, T. Xiong, H. Qu, J.J. Koh, D.K. Nandakumar, J. Wang, S. C. Tan, Manipulating unidirectional fluid transportation to drive sustainable solar water extraction and brine-drenching induced energy generation, *Energy Environ. Sci.* 13 (2020) 4891–4902.
- [65] P. Zhang, J. Li, L. Lv, Y. Zhao, L. Qu, Vertically aligned graphene sheets membrane for highly efficient solar thermal generation of clean water, *ACS Nano* 11 (2017) 5087–5093.
- [66] X. Li, W. Xu, M. Tang, L. Zhou, B. Zhu, S. Zhu, J. Zhu, Graphene oxide-based efficient and scalable solar desalination under one sun with a confined 2D water path, *Proc. Natl. Acad. Sci. USA* 113 (2016) 13953–13958.
- [67] L. Zhu, T. Ding, M. Gao, C.K.N. Peh, G.W. Ho, Shape conformal and thermal insulative organic solar absorber sponge for photothermal water evaporation and thermoelectric power generation, *Adv. Energy Mater.* 9 (2019), 1900250.
- [68] Y. Zhang, T. Xiong, L. Suresh, H. Qu, X. Zhang, Q. Zhang, J. Yang, S.C. Tan, Bioassay-directed isolation of antibacterial metabolites from an arthropod-derived Penicillium chrysogenum, *J. Nat. Prod.* 83 (2020) 3397–3403.
- [69] Y. Zhang, S.K. Ravi, S.C. Tan, Food-derived carbonaceous materials for solar desalination and thermo-electric power generation, *Nano Energy* 65 (2019), 104006.